Electronic Supplementary Material (ESI) for ChemComm.

Electronic Supplementary Information for

Operando mechanistic and dynamic studies of N/P co-doped hard carbon nanofibers for efficient sodium storage

Liaoliao Wang,[a] Juan Wang,[a] Dickon H. L. Ng,[b] Sheng Li,[a] Bobo Zou,[a] Yingxue Cui,[a] Xianhu Liu,[c] Sherif A. El−Khodary,[a] Jingxia Qiu[a] and Jiabiao Lian*[,a]

[a] Institute for Energy Research, Jiangsu University, Zhenjiang 212013, P. R. China

[b] Department of Physics, The Chinese University of Hong Kong, Shatin, Hong Kong, China

[c] Key Laboratory of Materials Processing & Mold (Zhengzhou University), Ministry of Education, Zhengzhou University, Zhengzhou, 450002, China.

* Corresponding author: Tel/Fax: 0086−511−88799500. *E-mail address*: jblian@ujs.edu.cn.

EXPERIMENTAL SECTION

Synthesis of the N/P-HCNF. Typically, 1.0 g polyacrylonitrile (PAN, average MW = 150000), 0.5 g triphenylphosphine (TPP), and 1.5 g $Zn(CH_3COO)_2{\cdot}2H_2O$ were dissolved in 12 mL of N, N-dimethylformamide (DMF) under magnetic stirring to form a homogeneous solution. Then, the solution was shifted into a 10 mL plastic syringe for electrospinning. The applied voltage was 13 kV, the constant ejection rate was 1.0 mL h^{-1}, and the distance between the needle tip and Al foil collector was 12 cm. The electrospined PAN/TPP/$Zn(Ac)_2$ film was collected and dried at 80 °C for 8 h. Thereafter, the electrospined film was put into ethanol solution (200 mL) containing 2-methylimidazole (0.65 g) and kept for 12 h at 25 °C. After drying at 60 °C for 6 h, the resultant film was pre-oxidized at 250 °C for 3 h in an air atmosphere and then calcined at 800 °C for 3 h under high-purity nitrogen (200 sccm) to obtain the final carbon nanofibers (N/P-HCNF).

Synthesis of the N-HCNF. The synthesis procedure of the N-HCNF material was similar to that of N/P-HCNF, without adding 0.5 g TPP in the electrospinning solution.

Synthesis of the HCNF. The synthesis procedure of the HCNF material was similar to that of N-HCNF, without further reaction with 2-methylimidazole.

Characterizations. FESEM (JEOL, JSM-7800F) and HRTEM (JEM-2100F) were performed to observe the morphology and microstructure of the carbon nanofibers. Elemental mappings were carried out based on the energy spectroscopy attached to the FESEM. The crystal structure of the carbon nanofibers was examined by using XRD (German Bruker D8 with Cu Kα). FTIR (Thermo Fisher Scientific Nicolet iS50, USA) was employed to study the chemical structure of the carbon nanofibers. The chemical composition and state of the carbon nanofibers were

characterized by XPS (ESCALAB 250Xi). The Brunauer–Emmette–Teller (BET) specific surface area and pore size distribution were evaluated by a Micromeritics Tristar II 3020 surface area analyzer at 77 K. Raman spectra and *in-situ* Raman spectra were recorded on a Zolix RTS2 Confocal Laser Raman microscope at the excitation wavelength of 532 nm. The Leitz microscope was fitted with an Olympus objective (50 × magnification). The operando spectroelectrochemical cell with a hole diameter of 5.5 mm and a 1.0 mm thick Quartz glass window was provided by the Beijing Scistar Technology Co. Ltd. *In-situ* Raman spectra (acquisition time of 30 s for each) were collected at different potentials during the discharge-charge process at a current density of 0.1 A g^{-1}.

Fabrication of Na metal half-cells. CR2032-type coin cells were assembled in an Ar-filled glove box (both H_2O and O_2 content < 0.1 ppm). The working electrodes were fabricated by using the mixed slurries of the active materials (80 wt.%), polyvinyldifluoride binder (10 wt.%), and super-P carbon black (10 wt.%) in N-methylpyrrolidone (NMP) solvent. The electrode area is 1 cm × 1 cm, and the mass loading of active materials was around 1.0 mg cm^{-2}. Copper foil, Na metal foil, and Whatman glassfiber was as the collector, counter/reference electrode, and separator, respectively. The electrolyte was 1.0 M $NaClO_4$ solution in a mixture of ethylene carbonate (EC) and dimethyl carbonate (DMC) (1:1 by volume) with 5% fluoroethylene carbonates (FEC) as the additive.

Electrochemical measurements. CV and EIS measurements were performed on the Gamry Interface 1000E electrochemical workstation. CV tests at various scan rates were recorded in the potential window of 0.01–3.0 V (vs. Na^+/Na), and EIS tests were conducted in the range of 100 kHz–0.01 Hz with 5.0 mV for amplitude. GCD and GITT measurements were carried out on

the LAND CT2001A battery tester. GITT tests were recorded at 0.1 A g^{-1} with a current pulse duration of 5 min and rest interval time of 1.0 h. The Na^+ diffusion coefficients (D_{Na+}) were calculated according to Fick's second law: $D_{Na+} = 4 (m_B V_M \Delta E_S)^2/\pi\tau (M_B S \Delta E_\tau)^2$, where τ is the pulse duration, m_B, V_M, and S are the active mass, molal volume, and geometric area of the electrode, M_B is the molar mass of carbon, ΔE_S and ΔE_τ are the potential variations during the rest and duration time.

Calculations of Warburg factor (σ) and Na^+ diffusion coefficients (D_{Na+}) based on EIS. According to the equation of $Z_W = \sigma\omega^{-1/2} - j\sigma\omega^{-1/2}$ ($\sigma\omega^{-1/2}$ and $-j\sigma\omega^{-1/2}$ represents real part Z' and imaginary part Z'', respectively), the Warburg factor (σ) can be determined by fitting Z' versus $\omega^{-1/2}$ in the low-frequency Z_W region. The D_{Na+} of the electrodes can be determined by the following formula of $D_{Na^+} = R^2T^2/2A^2n^4F^4C^2\sigma^2$, in which R is the gas constant, T is the absolute temperature of the test environment (298.15 K), A is the electrode area, n is the electron transfer number, F is the Faraday constant, C is the bulk concentration of Na^+.

Fig. S1 Schematic illustration of the fabrication process of the N/P-HCNF. (a) The synthesis process of the 1D carbon and (b) formation process of the multiscale pore structure.

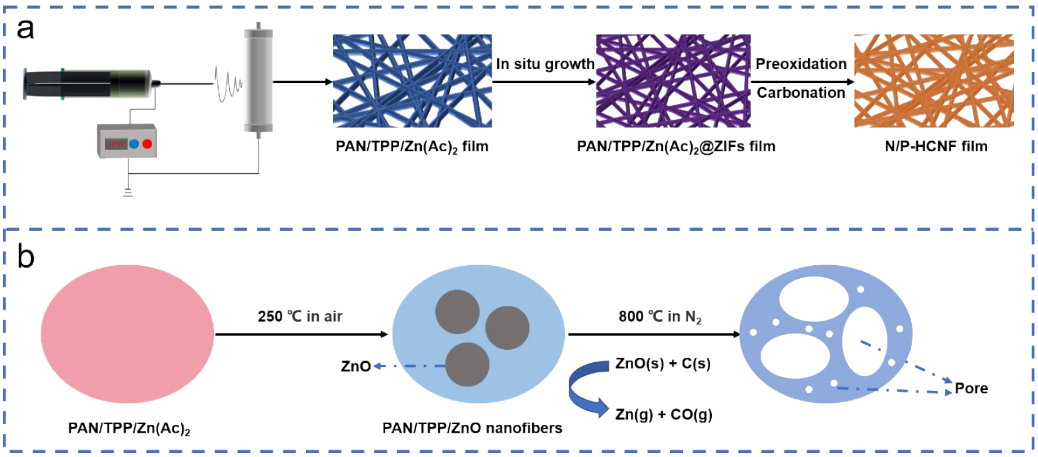

Fig. S1 shows a schematic illustration of a route for the synthesis of N/P-doped porous carbon nanofibers. Firstly, polyacrylonitrile (PAN), zinc acetate $Zn(Ac)_2$, and triphenylphosphine (TPP) were dissolved in the dimethylformate (DMF) solvent. Thereafter, zinc acetate $Zn(Ac)_2$ and the triphenylphosphine (TPP) solution were uniformly stirred and mixed with the PAN solution until a homogeneous electrospinning solution was obtained. By a simple electrospinning approach, the PAN/TPP/$Zn(Ac)_2$ composite nanofibers can be easily produced. The composite nanofiber films were then put into the ethanol solution containing 2-methyl-imidazole. After 12 h at room temperature, the forceful coordination of 2-methylimidazole to Zn^{2+} ions generated a layer of metallic imidazolate framework (MZIF; ZIF represents the zeolitic imidazolate framework, a class of MOFs) that would be coated onto the composite nanofibers.[1] This reaction was kinetically self-limiting. Afterward, both the 2-methylimidazole in ethanol solution and the metal acetate inside the core of the composite nanofibers could not be further reacted through the newly formed MZIF layer, thus giving rise to the PAN/TPP/$Zn(Ac)_2$@MZIF (M stands for metal) core-shell composite structure (Fig. S1a).

The as-spun PAN/TPP/$Zn(Ac)_2$@MZIF were aged at 250 °C for 3 h in air and then treated at 800 °C for 3 h in the N_2 atmosphere in order to complete the carbonization and reduction process. The ZIF-8 (zinc coordinated by four imidazolate rings) enables high N doping of a porous carbon structure and TPP(triphenylphosphine) provides phosphorus source. The PAN core transforms into carbon that can be etched by ZnO from the decomposition product of $Zn(Ac)_2$ in the composite fiber core, as shown in Fig. S1b, according to the carbothermal reduction $ZnO + C \rightarrow Zn + CO_2$ or CO.[2,3] In this pyrolysis process, the release of Zn vapors and other gases (CO, CO_2, etc.) produces a lot of pores, forming N/P-HCNF. For comparison, N-HCNF and HCNF were prepared by the same method and annealing conditions, respectively.

Fig. S2 (a) Nitrogen adsorption-desorption isotherm and (b) pore size distribution of the HCNF and N-HCNF samples.

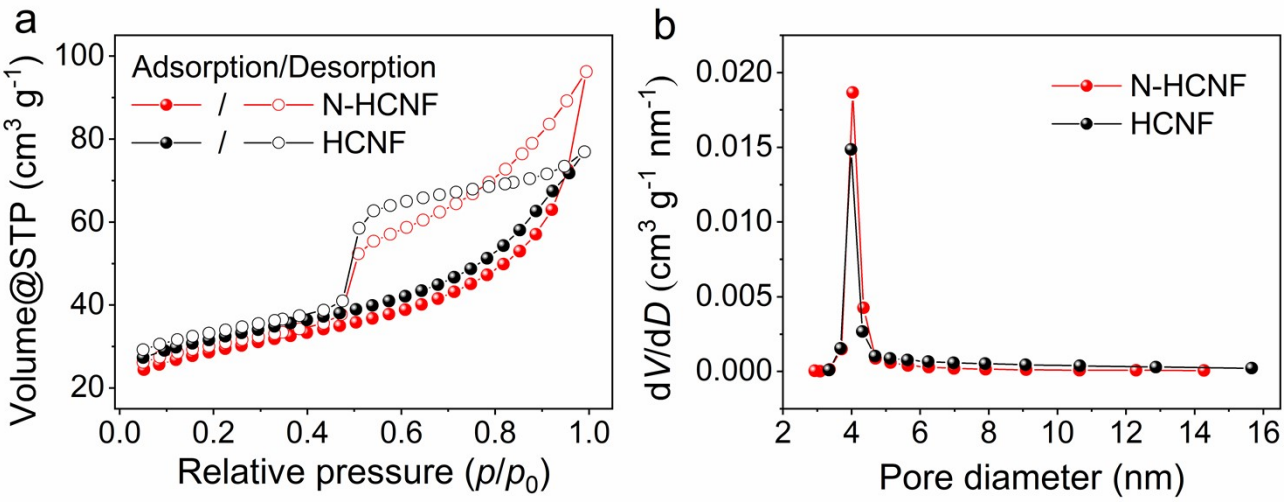

The Brunauer–Emmett–Teller (BET) surface area and pore volume were measured to be 76.95 m^2 g^{-1} and 0.07 cm^3 g^{-1} for HCNF, and 96.22 m^2 g^{-1} and 0.08 cm^3 g^{-1} for N-HCNF, respectively.

Fig. S3 (a) FESEM image with (b–e) the corresponding element mappings of the N/P-HCNF sample.

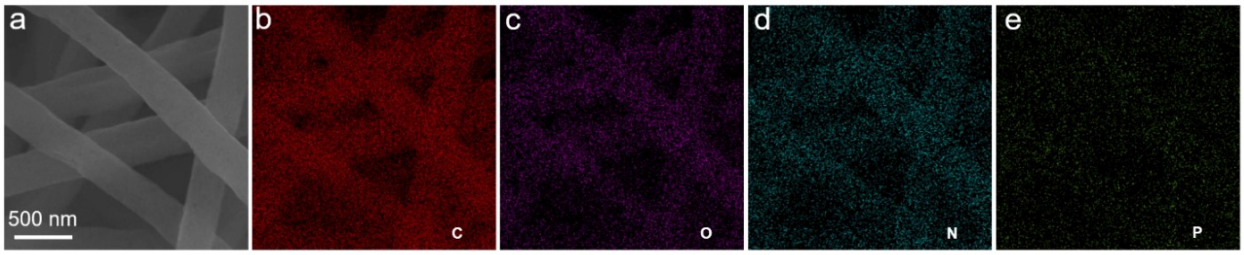

Fig. S4 SEM, TEM, and HRTEM images of the N-HCNF (a, b, c, and d) and HCNF (e, f, g, and h) samples, respectively.

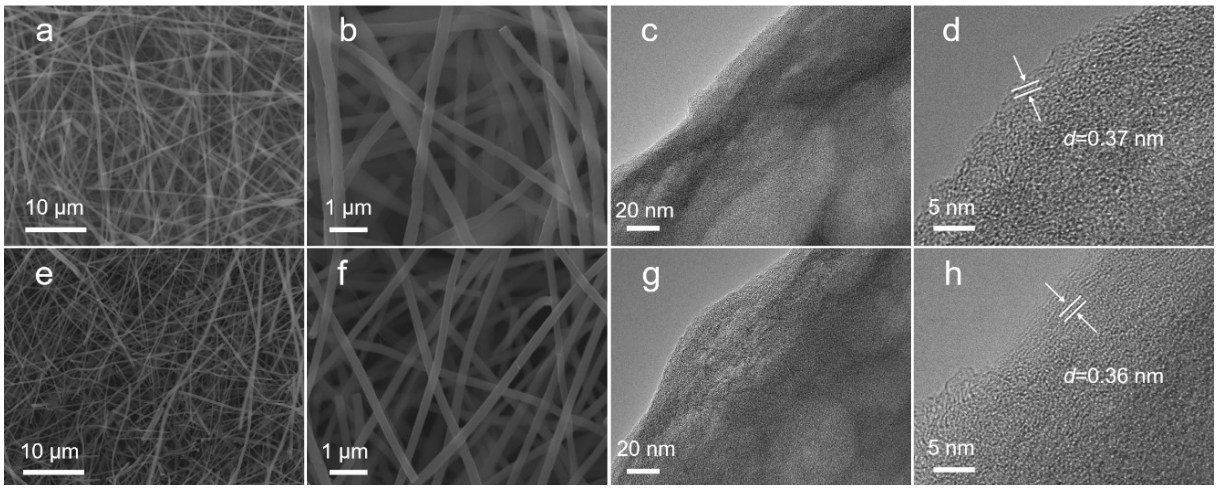

Fig. S5 (a) XRD patterns and (b) Raman spectra of the HCNF, N-HCNF, and N/P-HCNF samples, respectively.

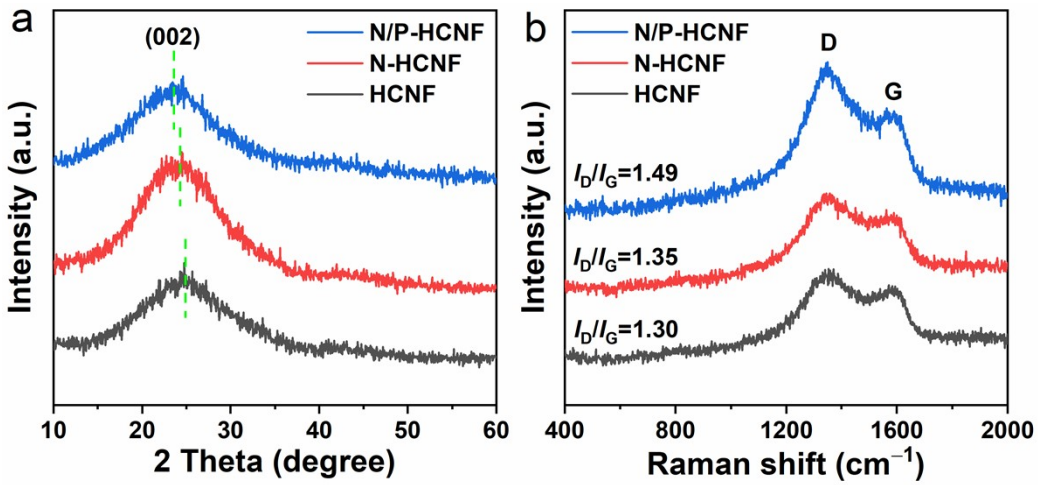

The XRD pattern of the N/P-HCNF (the upper curve of Fig. S5a) exhibited two weak and broad peaks, further indicating its disordered structure with a low degree of graphitization. The characteristic peak of the (002) plane around 23.4° corresponds to the lattice spacing $d_{(002)}$ of 0.38 nm, which was in well line with the HRTEM result. The Raman spectrum of the N/P-HCNF (the upper curve of Fig. S5b) displayed two characteristic peaks at 1358 cm^{-1} (D band) and 1590 cm^{-1} (G band), which were ascribed to the A_{1g} breathing-mode vibrations of C_6 rings at edges/defects and the E_{2g} vibrational mode vibrations of in-plane sp^2–hybridized C–C, respectively. Moreover, the intensity ratio of the D and G band (I_D/I_G) stands for the disordering degree, and the I_D/I_G value of the N/P-HCNF was calculated to be 1.49. Compared to the N/P-HCNF, both the N-HCNF and HCNF exhibited smaller $d_{(002)}$ spacing and lower I_D/I_G value. These results indicated that the N/P co-doping could expand the lattice spacing and introduce more defects, which are beneficial for the Na ions diffusion and storage. All the aforementioned merits would synergically make the N/P-HCNF boost superior sodium storage performance.

Fig. S6 Initial three CV curves at 0.1 mV s^{-1} and GCD curves at 0.1 A g^{-1} of the N/P-HCNF (a, b), N-HCNF (c, d), and HCNF (e, f) anodes, respectively.

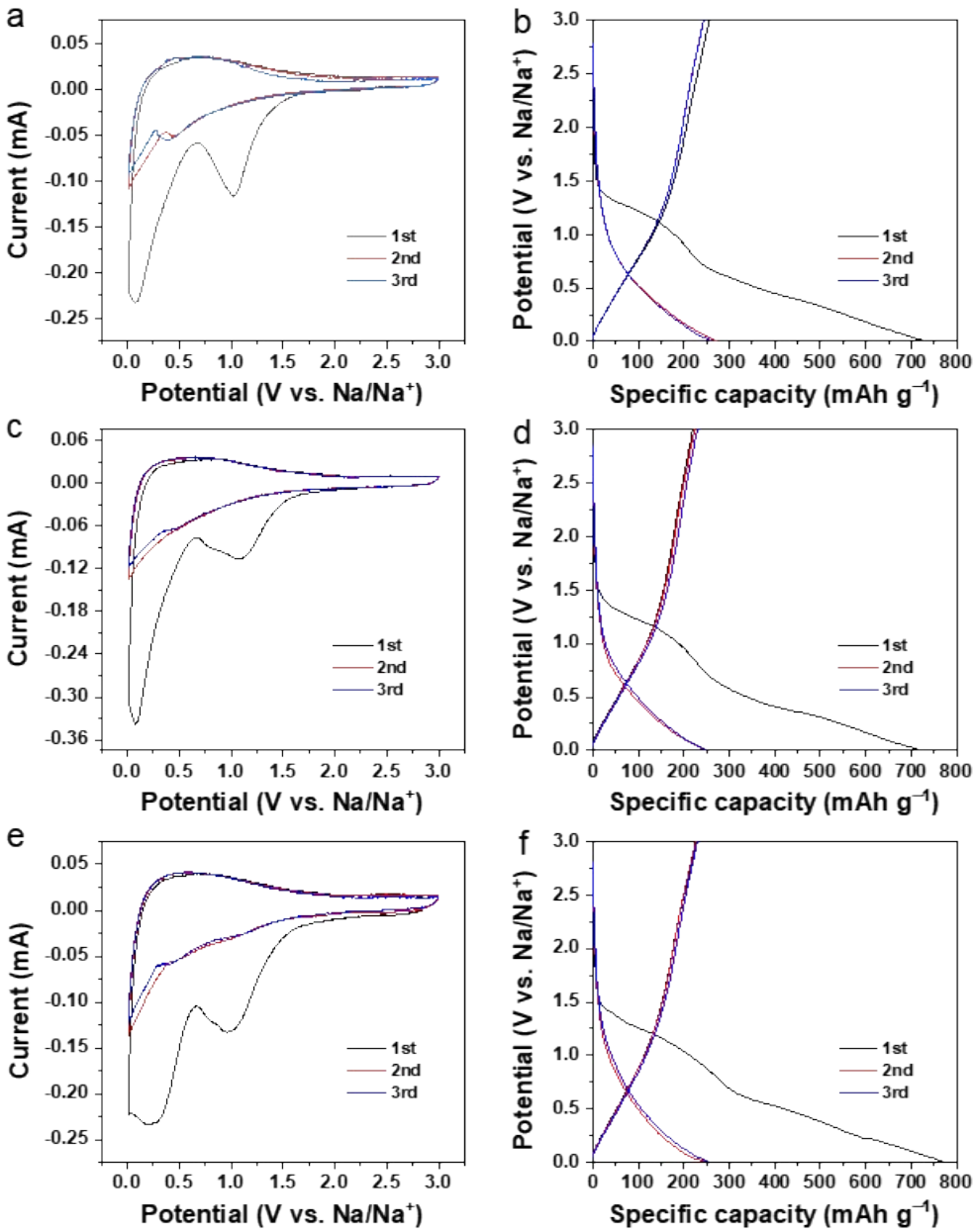

Fig. S7 CV curves at the scan rates of 0.1–5.0 mV s^{-1}, the fitting of *b*-value, surface capacitive contribution at 1.0 mV s^{-1}, and contribution ratios of the surface capacitive and diffusive processes at different scan rates of the N/P-HCNF (a–d), N-HCNF (e–h), and HCNF (i–l) electrodes, respectively.

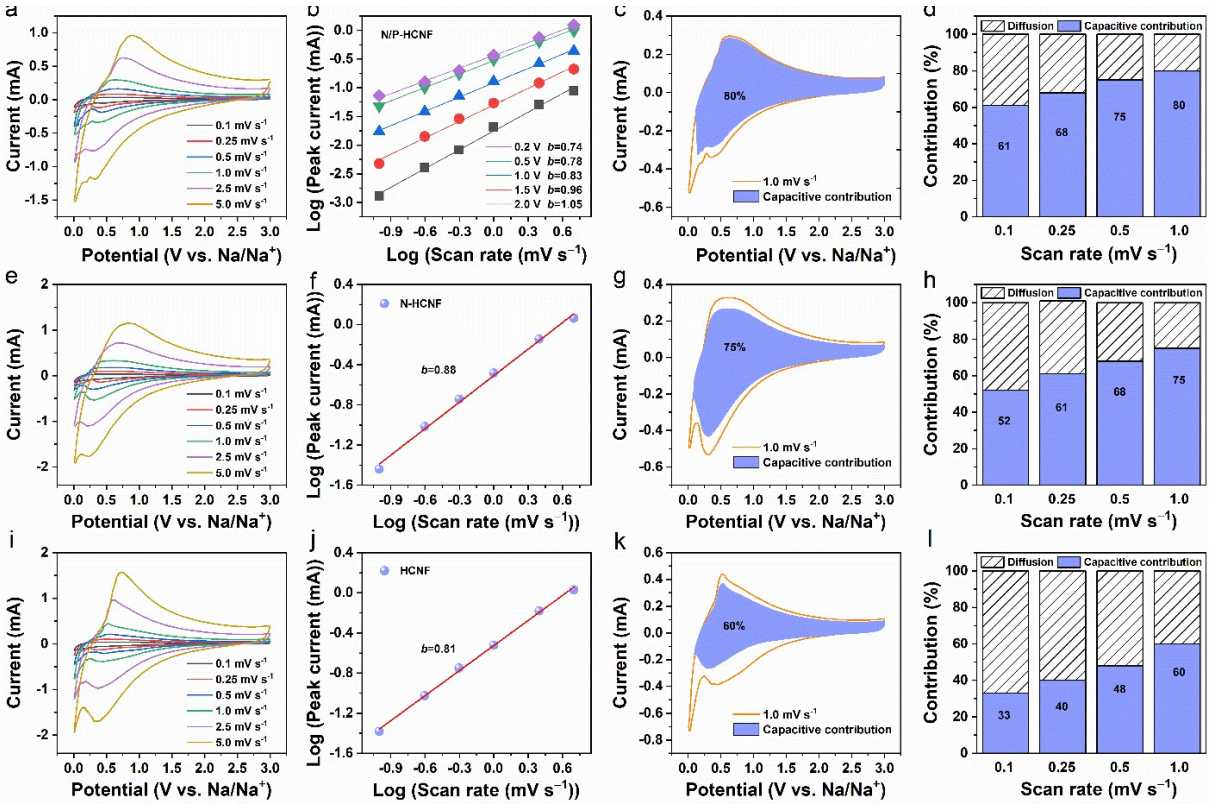

The Na^+ storage kinetics of the electrodes was investigated based on their CV profiles at various scan rates of 0.1–5.0 mV s^{-1} (Fig. S7). In general, the peaks current (*i*) is proportional to the scan rate (*v*) obeying the power-law equation of $i = kv^b$. The *b*-value of 1.0 or 0.5 represents the capacity contribution behavior dominated by surface capacitive or diffusion-controlled process, respectively. From the slope of log(*i*) against log(*v*) (Fig. S7a), the *b*-value was determined to be 1.05, 0.98, 0.85, 0.81, and 0.76 at 2.0, 1.5, 1.0, 0.5, and 0.2 V, respectively. The results implied that the Na^+ storage at the higher potential region was dominated by

capacitive behavior, which was favorable for achieving superior rate performance. Furthermore, a quantitative ratio of capacitive and diffusive contributions can be calculated by separating the current (i) at a specific potential as $i(v) = k_1v + k_2v^{1/2}$. Accordingly, the capacitive contribution (shaded area in Fig. S7c) of the N/P-HCNF at 1.0 mV s^{-1} was estimated to be 80%. As shown in Fig. S7d, the proportion of the capacitive contribution was steadily up from 61% to 80% as the increasing scan rate from 0.1 to 1.0 mV s^{-1}, illustrating that the fast surface capacitive behavior dominated the Na^+ storage of the N/P-HCNF, especially at high current densities. Meanwhile, kinetics analysis was also conducted on the N-HCNF (Fig. S7e–h) and HCNF (Fig. S7i–l). By comparison with the kinetic information of the N/P-HCNF, it was evident that the N/P co-doping can improve the capacitive behavior to boost fast Na^+ storage kinetics.

Fig. S8 Cycling performance of the N-HCNF and HCNF electrodes at 1.0 A g^{-1}.

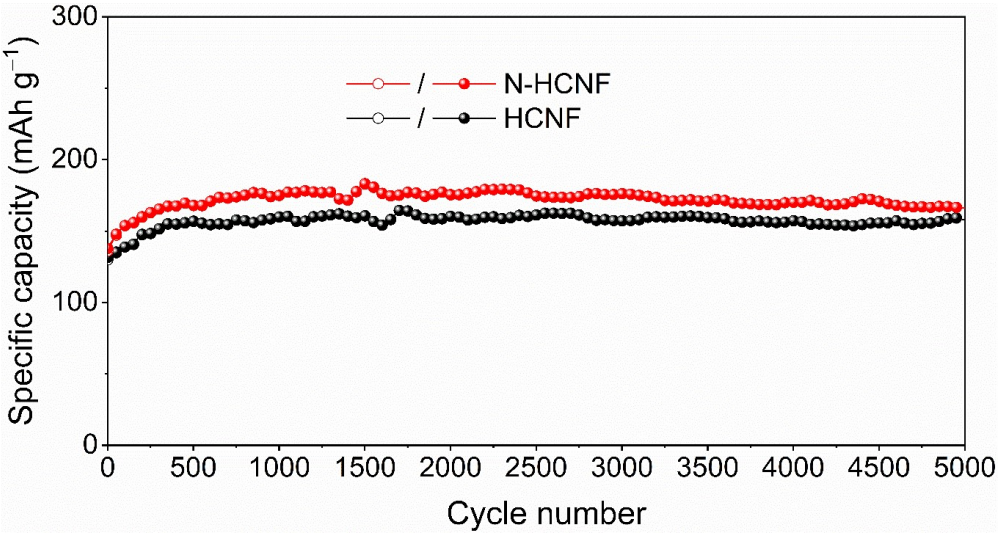

Table S1 Electrochemical performance of our N/P-HCNF in comparison with previously reported

Anode Materials [ref.]	Potential (V vs. Na/Na^+)	Reversible Specific Capacity and Rate Capability	Cycle Performance
This work	**0.01–3.0**	**271 mAh g^{-1} at 0.1 A g^{-1} 100 mAh g^{-1} at 10 A g^{-1}**	**95% after 5000 cycles at 1.0 A g^{-1}**
SC-NS[4]	0.01–3.0	232 mAh g^{-1} at 0.02 A g^{-1} 103 mAh g^{-1} at 1.0 A g^{-1}	93% after 3500 cycles at 0.8 A g^{-1}
NDCNFs[5]	0.001–2.5	293 mAh g^{-1} at 0.05 A g^{-1} 150 mAh g^{-1} at 1.0 A g^{-1}	93.7% after 200 cycles at 1.0 A g^{-1}
N-CNFS[6]	0.001–2.5	293 mAh g^{-1} at 0.05 A g^{-1} 159 mAh g^{-1} at 1.0 A g^{-1}	87% after 200 cycles at 0.05 A g^{-1}
S-N/C[7]	0.01–3.0	300 mAh g^{-1} at 0.1 A g^{-1} 110 mAh g^{-1} at 10.0 A g^{-1}	96% after 1000 cycles at 1.0 A g^{-1}
NCNFs-IWNC[8]	0.0–3.0	290 mAh g^{-1} at 0.1 A g^{-1} 148 mAh g^{-1} at 10.0 A g^{-1}	98% after 5000 cycles at 5.0 A g^{-1}
NSC-SP[9]	0.01–3.0	280 mAh g^{-1} at 0.03 A g^{-1} 130 mAh g^{-1} at 10.0 A g^{-1}	97% after 3400 cycles at 0.5 A g^{-1}
S-HC-p[10]	0.01–3.0	340 mAh g^{-1} at 0.1 A g^{-1} 117 mAh g^{-1} at 10.0 A g^{-1}	92% after 4000 cycles at 1.0 A g^{-1}
HAT-CNFs[11]	0.01–3.0	395 mAh g^{-1} at 0.1 A g^{-1} 106 mAh g^{-1} at 10.0 A g^{-1}	95% after 500 cycles at 0.5 A g^{-1}
FN-CNFs[12]	0.01–2.0	150 mAh g^{-1} at 0.2 A g^{-1} 87 mAh g^{-1} at 10.0 A g^{-1}	89% after 200 cycles at 0.2 A g^{-1}
NMC[13]	0.001–3.0	209.5 mAh g^{-1} at 0.1 A g^{-1} 48.9 mAh g^{-1} at 2.0 A g^{-1}	94% after 800 cycles at 0.5 A g^{-1}
NCNAs[14]	0.01–2.5	335 mAh g^{-1} at 0.1 A g^{-1} 110 mAh g^{-1} at 3.0 A g^{-1}	91% after 500 cycles at 0.1 A g^{-1}
FNGP[15]	0.01–3.0	197 mAh g^{-1} at 0.05 A g^{-1} 50 mAh g^{-1} at 1.0 A g^{-1}	89% after 5000 cycles at 1.0A g^{-1}

hetero-atomic doped carbon materials.

References

1 W. Zhang, Z.-Y. Wu, H.-L. Jiang and S.-H. Yu, *J. Am. Chem. Soc.* 2014, **136**, 14385–14388.

2 J. E. Jin, J.-H. Lee, J. H. Choi, H.-K. Jang, J. Na, D. Whang, D.-H. Kim and G.-T. Kim, *Phys. Chem. Chem. Phys.* 2016, **18**, 101–109.

3 Y. Chen, X. Li, K. Park, W. Lu, C. Wang, W. Xue, F. Yang, J. Zhou, L. Suo, T. Lin, H. Huang, J. Li and J. B. Goodenough, *Chem* 2017, **3**, 152–163.

4 X. Yao, Y. Ke, W. Ren, X. Wang, F. Xiong, W. Yang, M. Qin, Q. Li and L. Mai, *Adv. Energy Mater*. 2018, ***9***, 1803260.

5 J. D. Zhu, C. Chen, Y. Lu, Y. Q. Ge, H. Jiang, K. Fu and X. W. Zhang, *Carbon* 2015, **94**, 189–195.

6 J. Zhu, C. Chen, Y. Lu, Y. Ge, H. Jiang, K. Fu and X. Zhang, *Carbon* 2015, ***94***, 189–195.

7 J. Q. Yang, X. L. Zhou, D. H. Wu, X. D. Zhao and Z. Zhou, *Adv. Mater.* 2016, **38**, 1604108.

8 W. X. Zhao, X. Hu, S. Q. Ci, J. X. Chen, G. X. Wang, Q. H. Xu and Z. H. Wen, *Small* 2019, **15**, 1904054.

9 D. Xu, C. Chen, J. Xie, B. Zhang, L. Miao, J. Cai, Y. Huang and L. Zhang, *Adv. Energy Mater.* 2016, **6**, 1501929.

10 Z. H. Hong, Y. C. Zhen, Y. R. Ruan, M. L. Kang, K. Q. Zhou, J. M. Zhang, Z. G. Huang and M. D. Wei, *Adv. Mater.* 2018, **29**, 1802035.

11 R. Y. Yan, E. Josef, H. J. Huang, K. Leus, M. Niederberger, J. P. Hofmann, R. Walczak, M. Antonietti and M. Oschatz, *Adv. Funct. Mater*. 2019, **39**, 1902858.

12 Z. Wang, L. Qie, L. Yuan, W. Zhang, X. Hu and Y. Huang, *Carbon* 2013, **55**, 328–334.

13 H. Liu, M. Jia, N. Sun, B. Cao, R. J. Chen, Q. Z. Zhu, F. Wu, N. Qiao and B. Xu, *ACS Appl. Mater. Interfaces* 2015. **49**, 27124–27130.

14 D. Xie, J. Zhang, G. Pan, H. Li, S. Xie, S. Wang, H. Fan, F. Cheng and X. Xia, *ACS Appl. Mater. Interfaces* 2019, **11**, 18662–18670.

15 H. An, Y. Li, Y. Gao, C. Cao, J. Han, Y. Feng and W. Feng, *Carbon* 2017, **116**, 338–346.